Superconductivity in PtPb$_4$ with possible nontrivial band topology

C. Q. Xu,[1,2] B. Li [ORCID],[3] L. Zhang,[2] J. Pollanen [ORCID],[2] X. L. Yi,[1] X. Z. Xing,[1] Y. Liu,[4] J. H. Wang [ORCID],[5] Zengwei Zhu,[5] Z. X. Shi,[1,*]
Xiaofeng Xu [ORCID],[4,†] and X. Ke[2,‡]

[1]*School of Physics and Key Laboratory of MEMS of the Ministry of Education, Southeast University, Nanjing 211189, China*
[2]*Department of Physics and Astronomy, Michigan State University, East Lansing, Michigan 48824-2320, USA*
[3]*Information Physics Research Center, Nanjing University of Posts and Telecommunications, Nanjing 210023, China*
[4]*Key Laboratory of Quantum Precision Measurement of Zhejiang Province, Department of Applied Physics,*
Zhejiang University of Technology, Hangzhou 310023, China
[5]*Wuhan National High Magnetic Field Center, School of Physics, Huazhong University of Science and Technology, Wuhan 430074, China*

Superconductivity in topological quantum materials is much sought after, as it represents the key avenue to searching for topological superconductors, which host a full pairing gap in the bulk but Majorana bound states at the surface. To date, however, the simultaneous realization of nontrivial band topology and superconductivity in the same material under ambient conditions remains rare. In this paper, we study both superconducting and topological properties of the binary compound PtPb$_4$ ($T_c \sim 2.7$ K) that was recently reported to exhibit large Rashba splitting, inherent to the heavy $5d$ Pt and $6p$ Pb. We show that in PtPb$_4$, the specific heat jump at T_c reaches $\Delta C/\gamma T_c \sim 1.70 \pm 0.04$, larger than the 1.43 expected for weak-coupling BCS superconductors. Moreover, the measurement of quantum oscillation suggests the possibility of a topological band structure, which is further studied by density functional theory calculations. Our study may stimulate future experimental and theoretical investigations in this intriguing material.

I. INTRODUCTION

Following the advent of topological insulators, the search for topological quantum materials with diverse symmetry-enforced topological states, characterized by nontrivial topological invariants, has attracted a flurry of research interest in both condensed-matter physics and materials science [1,2]. For instance, both three-dimensional (3D) Dirac semimetals with fourfold degenerate band crossings and Weyl semimetals with pairs of Weyl nodes due to broken inversion symmetry or time-reversal symmetry have been demonstrated to exhibit extraordinary physical properties, such as an extremely large magnetoresistance (MR), an ultrahigh carrier mobility, and a chiral anomaly induced negative MR [3–14]. Another prominent example is the topological nodal-line semimetals in which Dirac bands cross along a one-dimensional trajectory (line or loop) in momentum space, in contrast to the isolated Dirac nodes in topological insulators and Dirac semimetals. Thus far, topological nodal-line states have been theoretically predicted and experimentally validated in some compounds, such as ZrSiS [15–18], PbTaSe$_2$ [19,20], and PtSn$_4$ [21,22].

Among these topological materials, those showing superconductivity at low temperatures are particularly intriguing since they provide arguably a natural platform to realize Majorana fermions, the manipulation of which forms the basis of future topological quantum computing. Majorana fermions are exotic particles which represent their own antiparticles and

can arise in some novel physical systems, e.g., in the vortex core of topological superconductors [23]. Arguably, superconductors with odd-parity pairing (e.g., UPt$_3$ [24], Cu$_x$Bi$_2$Se$_3$ [23]) or broken time-reversal symmetry (e.g., chiral LaPt$_3$P [25]) are strong candidates for topological superconductors [26]. Nevertheless, these odd-parity or chiral superconductors are either rare or sensitive to disorder, and as such the ambiguous evidence for topological superconductivity is still elusive. Another feasible route to realize topological superconductors is to search for intrinsic superconductivity in topological materials, either in stoichiometric compounds at ambient or under high pressure or by doping the topological materials to tune the superconductivity. Indeed, superconductivity achieved in this manner has been observed in Cu$_x$Bi$_2$Se$_3$ [23,27,28], Au$_2$Pb [29,30], PbTaSe$_2$ [31], β-PdBi$_2$ [32,33], S-doped MoTe$_2$ [34], etc., and in some cases, experimental evidence of Majorana zero modes has been claimed.

In this broad context, the binary PtPb$_4$, a homologue of the Dirac nodal arc semimetal PtSn$_4$, was recently reported to exhibit large Rashba splitting around the Γ point by ARPES [35], which is inherent to the large atomic numbers of both Pt and Pb. PtPb$_4$ is particularly interesting, as it also superconducts below $T_c \sim 2.7$ K [35,36], whereupon it is likely to be a candidate for a topological superconductor. Despite its superconductivity having been reported a few decades ago, a detailed study of its superconducting properties, in particular, its association with putative topological states, is still lacking.

In this article, we report the synthesis of high-quality PtPb$_4$ single crystals and a detailed study of their transport and thermodynamic properties by means of resistivity, magnetization, and heat capacity measurements. We study the

*zxshi@seu.edu.cn
†xuxiaofeng@zjut.edu.cn
‡kexiangl@msu.edu
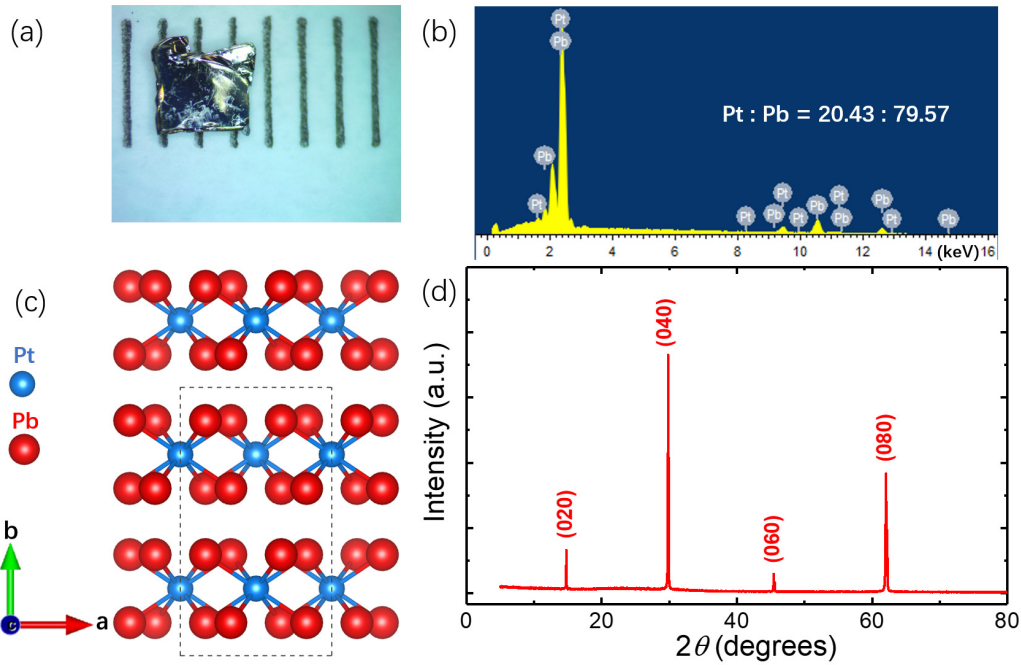
FIG. 1. (a) The optical view of a single crystal used in this study. (b) Energy-dispersive x-ray spectroscopy of a typical sample. (c) Schematic crystal structure of PtPb$_4$. (d) X-ray diffraction pattern from the basal plane of a cleaved crystal, showing only (0 *l* 0) reflections.

superconducting properties of PtPb$_4$ by measuring its lower and upper critical fields and investigate the possible topological properties by the de Haas–van Alphen (dHvA) oscillations and first-principles calculations.

II. EXPERIMENTAL DETAILS

Large PtPb$_4$ single crystals, up to several millimeters long, were synthesized by the self-flux method [35]. Accurately weighed high-purity platinum pieces and lead shots were mixed at the molar ratio of 11:89. The mixed materials were placed in an alumina crucible and sealed in an evacuated quartz tube. The quartz tube was subsequently loaded into a box-type furnace, heated to 700°C over a period of 10 h, and then kept at this temperature for 1 day to ensure complete melting. Afterwards, the furnace temperature was gradually cooled to 310°C (at a rate of 1°C/h), at which temperature the quartz tube was removed from the furnace and was immediately centrifuged to get rid of the excess flux. The resulting shiny PtPb$_4$ single crystals obtained had lateral dimensions of several millimeters [as shown in Fig. 1(a)]. In order to eliminate contamination from the possible residual flux, we used freshly cleaved samples for all measurements.

Single-crystal x-ray diffraction measurements were conducted at room temperature using a Rigaku diffractometer to check the crystalline quality. The actual chemical composition of the as-grown single crystals was determined using a field-emission scanning electron microscope (Hitachi Regulus 8230) equipped with Oxford Ultim Extreme energy-dispersive x-ray spectroscope. The electrical resistivity, heat capacity, and magnetotransport measurements were carried out in a Quantum Design Physical Property Measurement System, and the magnetic susceptibility was measured in a Quantum Design Magnetic Property Measurement System.

We performed the electronic structure calculations using the generalized gradient approximation [37] as implemented in the full-potential linearized augmented plane-wave code WIEN2K [38]. The muffin tin radii were chosen to be 2.5 a.u. for all atoms. The plane-wave cutoff was defined by $R \cdot K_{max} = 7.0$, where R is the smallest atomic sphere radius in the unit cell and K_{max} is the magnitude of the largest K vector. To calculate the topological properties and Fermi surfaces (FSs), we projected the Hamiltonian onto a basis made of d Pt-centered and p Pb-centered orbitals, for a total of 136 Wannier functions, by means of the WANNIER90 and WannierTools packages [39,40]. The FSs were generated using a dense K-point mesh of $26 \times 15 \times 27$ in the Brillouin zone. The related angular dependence of the quantum oscillation frequencies was calculated using the SKEAF code [41]. Since both Pt and Pb are heavy elements, relativistic effects and spin-orbit coupling (SOC) were taken into account in all calculations.

III. RESULTS

Figure 1(b) shows the typical energy-dispersive x-ray spectroscopy result measured on an as-grown PtPb$_4$ single crystal. The actual chemical stoichiometry is determined to be Pt:Pb = 20.43:79.57, very close to the nominal composition. Figure 1(c) depicts the perspective of the crystal structure viewed along the c axis, suggesting its layered structure. While PtPb$_4$ was previously reported to crystalize in a *tetragonal* structure with the space group $P4/nbm$ (No. 125), Lee *et al.* recently found that it actually has an *orthorhombic* lattice structure with the space group $Ccca$ (No. 68) by carrying out a synchrotron x-ray diffraction study. It is conceivable that our crystals have the same structure as Lee *et al.*'s since almost the same procedures were used for crystal growth.
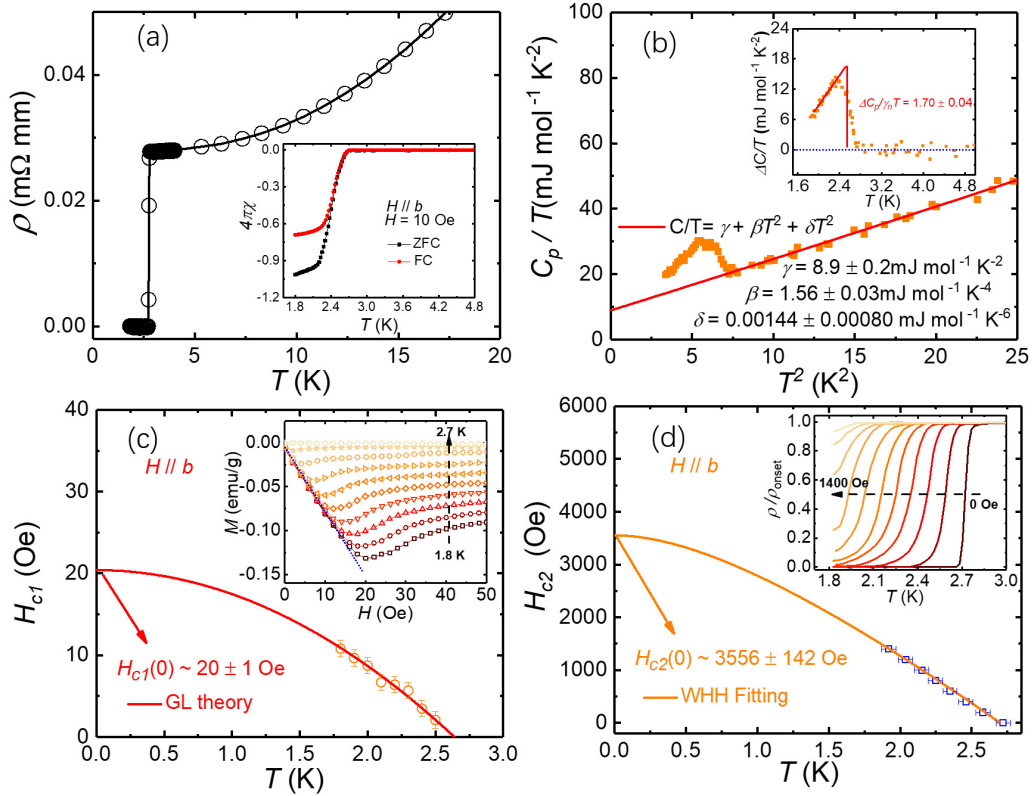
FIG. 2. (a) T dependence of resistivity measured under zero magnetic field. Inset: Magnetic susceptibility as a function of temperature at a field of $H = 10$ Oe in the zero-field-cooled (ZFC) and field-cooled (FC) modes, respectively. (b) The heat capacity C_p divided by the temperature T as a function of T^2 at low temperatures. The solid red line shows the fit to the data described in the text. Inset: $\Delta C/T$ versus T, where $\Delta C = C - C_n$, with C_n being the heat capacity of the normal state. (c) Temperature dependence of the lower critical field H_{c1} extracted from the inset. The solid red line is the fit using the Ginzburg-Landau (GL) formula. (d) T dependence of the upper critical field H_{c2} and its fit with the Werthamer-Helfand-Hohenberg (WHH) formula. Inset: The resistivity measured at various magnetic fields.

Following this newly determined orthorhombic crystal structure of PtPb$_4$ (i.e., the same as that of its sister compound PtSn$_4$), we present single-crystal diffraction data in Fig. 1(d), where only $(0\ l\ 0)$ peaks are observable and no extra impurity phases are detectable, confirming the high quality of our crystals.

Figure 2(a) illustrates the temperature (T) dependence of zero-field resistivity, with the inset showing the magnetic susceptibility under both the zero-field-cooled (ZFC) and the field-cooled (FC) protocols. It is notable that PtPb$_4$ exhibits metallic behaviors at high temperatures and undergoes a sharp superconducting transition below the critical temperature $T_c \sim 2.7$ K, in good agreement with a previous report [36]. The residual resistivity ratio, $\rho_{300\,\mathrm{K}}/\rho_{3\,\mathrm{K}}$, is approximately 50, indicative of a high degree of metallicity. Both ZFC and FC magnetization curves show a large diamagnetic susceptibility upon the superconducting transition. Bulk superconductivity is also evident from the low-T heat capacity data measured at zero magnetic field [Fig. 2(b)], where a λ-shaped anomaly is clearly observed at T_c. The solid red curve in Fig. 2(b) represents the fit to the normal-state heat capacity and its extrapolation to low temperatures. The normal-state heat capacity is modeled with

$$C_p/T = \gamma_n + \beta T^2 + \delta T^4, \tag{1}$$

where the first term is the electronic term and the other two are phononic contributions. The fit yields $\gamma_n = (8.9 \pm 0.2)$ mJ/mol K^2, $\beta = (1.56 \pm 0.03)$ mJ/mol K^4, and $\delta = (0.001\,44 \pm 0.0008)$ mJ/mol K^6. The Debye temperature Θ_D is determined from the formula

$$\Theta_D = \left(\frac{12\pi^4}{5\beta} nR \right)^{1/3}, \tag{2}$$

where n is the number of atoms per formula unit, and $R = 8.31$ J/mol K^{-2} is the gas constant. The calculated Θ_D is (184 ± 5) K. In the inset in Fig. 2(b), we present the heat capacity anomaly $\Delta C/T$ after subtracting the normal-state background. The value $\Delta C/\gamma T_c$ is thus estimated as $\sim 1.70 \pm 0.04$, larger than the 1.43 that is expected for weak-coupling BCS superconductors. This $\Delta C/\gamma T_c$ value possibly results from enhanced electron-phonon coupling. Once the electron-phonon mechanism is assumed, the electron-phonon coupling constant λ_{e-p} can be independently evaluated via the modified McMillian formula [42,43],

$$\frac{\Delta C}{\gamma T_c} = 1.43 \left[1 + 53 \left(\frac{T_c}{\omega_{\ln}} \right)^2 \ln \left(\frac{\omega_{\ln}}{3T_c} \right) \right], \tag{3}$$

$$1.2 T_c = \omega_{\ln} \exp \left[\frac{-1.04(1+\lambda)}{\lambda - \mu^*(1+0.62\lambda)} \right], \tag{4}$$

where $\omega_{\ln}$ is the average phonon frequency, and $\mu^\star$ is the Coulomb pseudopotential and has a typical value of ~ 0.13. Based on the $\Delta C/\gamma T_c$ value obtained above, we find $\lambda_{e\text{-}p} = 0.83 \pm 0.04$. Here both $\lambda_{e\text{-}p}$ and $\Delta C/\gamma T_c$ are slightly larger than in many BCS superconductors and are very close to those in the intermediately coupled superconductors (e.g., indium, with $T_c = 3.4$ K, $\lambda_{e\text{-}p} = 0.81$) [43]. Alternatively, we can also derive $\lambda_{e\text{-}p}$ using the McMillan equation:

$$\lambda_{e\text{-}p} = \frac{1.04 + \mu^* \ln(\Theta_D/1.45 T_c)}{(1 - 0.62\mu^*)\ln(\Theta_D/1.45 T_c) - 1.04}. \quad (5)$$

With the Debye temperature obtained above, $\lambda_{e\text{-}p}$ is estimated to be 0.62.

The lower critical field H_{c1} with a magnetic field applied along the b axis (i.e., perpendicular to the basal plane) was studied by examining the M-H curves measured below T_c. As depicted in the inset in Fig. 2(c), the magnetization shows a linear dependence on the field below H_{c1} and it deviates from the linear slope above H_{c1}, characteristic of a type II superconductor. The extracted lower critical H_{c1} is plotted in Fig. 2(c). By fitting the data using the Ginzburg-Landau equation

$$H_{c1}(T) = H_{c1}(0)\left[1 - \left(\frac{T}{T_c}\right)^2\right], \quad (6)$$

we estimate $H_{c1}(0)$ as $\sim 20 \pm 1$ Oe at $T = 0$ K. Using the expression $\mu_0 H_{c1} = \frac{\phi_0}{4\pi\lambda^2}(\ln\frac{\lambda}{\xi})$ and the coherence length ξ derived below, the magnetic penetration depth is calculated to be $\lambda \sim (476.0 \pm 50.0)$ nm.

We also study the upper critical field H_{c2} by measuring the resistivity under various applied fields. As demonstrated in the inset in Fig. 2(d), the superconducting transition progressively shifts to lower temperatures and the width of the transition becomes broadened with increasing field. We determine the upper critical field H_{c2} by taking the points where the resistivity drops to 50% of its normal-state value right above T_c. The thus-determined H_{c2} as a function of the temperature is presented in Fig. 2(d), with the out-of-plane ($H \parallel b$) field direction. The solid curve in Fig. 2(d) represents the fit using the Werthamer-Helfand-Hohenberg (WHH) formula [44]. $H_{c2}(0)$ is thus estimated to be $\sim (3556 \pm 142)$ Oe, which is much smaller than the Pauli limit, suggesting the orbital effect at play here. Given $\mu_0 H_{c2} = \frac{\phi_0}{2\pi\xi^2}$, this gives the coherence length $\xi \sim (30.44 \pm 0.61)$ nm and the Ginzburg-Landau parameter $\kappa = \frac{\lambda}{\xi} \simeq 15.64 \pm 1.96$.

Figure 3(a) shows the resistivity ρ as a function of the temperature at various magnetic fields. As shown, $\rho(T)$ exhibits a weak upturn at low temperatures when the field approaches 9 T. The magnetoresistance, defined as MR $= \frac{\rho(H) - \rho(0)}{\rho(0)} \times 100\%$, has also been measured at various temperatures as shown in Fig. 3(b). The magnitude of the MR ($\sim 350\%$ at 9 T and 5 K) does not show any sign of saturation. Interestingly, we find that, by plotting MR vs B/ρ, all curves collapse on each other as shown in the inset in Fig. 3(b), which suggests that the MR behavior of PtPb$_4$ follows the semiclassical Kohler's rule. This feature has also been observed in topological WTe$_2$ [45], PdSn$_4$ [46], etc. We also measured the Hall effect to determine the carrier types in PtPb$_4$. As a routine

process, we antisymmetrize the data using $\rho_{xy} = \frac{\rho(+H) - \rho(-H)}{2}$. The Hall resistivity ρ_{xy} is displayed in Fig. 3(c). As noted, the Hall resistivity shows nonlinearity with the field, consistent with the multiband features as evidenced from both the quantum oscillations and the Fermi surface calculations, discussed later. Then we obtain the conductivity tensors σ_{xx} and σ_{xy} from the measured resistivity and Hall resistivity [47,48]:

$$\sigma_{xx} = \frac{\rho_{xx}}{\rho_{xx}\rho_{xx} + \rho_{xy}\rho_{xy}}, \quad \sigma_{xy} = -\frac{\rho_{xy}}{\rho_{xx}\rho_{xx} + \rho_{xy}\rho_{xy}}. \quad (7)$$

Afterward, we fit both the longitudinal (σ_{xx}) and the transverse (σ_{xy}) magnetoconductivity using the two-band model as parameterized below and the fits are illustrated in Fig. 3(e):

$$\sigma_{xx} = -e\left(\frac{n_e \mu_e}{1 + \mu_e^2 B^2} + \frac{n_h \mu_h}{1 + \mu_h^2 B^2}\right), \quad (8)$$

$$\sigma_{xy} = eB\left(\frac{n_e \mu_e^2}{1 + \mu_e^2 B^2} - \frac{n_h \mu_h^2}{1 + \mu_h^2 B^2}\right). \quad (9)$$

Here e is the elementary charge -1.602×10^{-19} C, and n_e and n_h are the carrier density and μ_e and μ_h are the corresponding mobility of electrons and holes, respectively. It is clearly shown that both σ_{xx} and σ_{xy} can be well fitted using this two-band model in the whole field range studied. The fitting gives $n_h = (1.45 \pm 0.11) \times 10^{27}$ m^{-3}, $n_e = (1.28 \pm 0.13) \times 10^{27}$ m^{-3}, $\mu_h = (0.52 \pm 0.05)$ m^2/V s, and $\mu_e = (0.48 \pm 0.05)$ m^2/V s at 5 K. However, given the number of free parameters used in the model, the good fitting shown here does not exclude other sets of parameters which may fit the data equally well.

To proceed, we study the electronic structure of PtPb$_4$ via quantum dHvA oscillations. The isothermal magnetization data with the magnetic field applied along the b axis are measured. After subtracting the polynomial background, we show in Fig. 4(a) the oscillatory signals measured at different temperatures up to 12 K. The oscillations appear under a field as low as 2.5 T at 1.9 K, indicating the good sample quality. The amplitude of oscillations decreases with increasing temperature. The fast Fourier transform (FFT) of the oscillatory magnetization ΔM shows two major frequencies, $F_\alpha = (45 \pm 11)$ T and $F_\beta = (160 \pm 9)$ T, shown in Fig. 4(b). Based on the Onsager relation $F = (\hbar/2\pi e)A_e$, we extracted the extremal FS cross-sectional area A_e associated with each frequency; for α, $A_e(\alpha) = (0.43 \pm 0.11)$ nm^{-2}; and for β, $A_e(\beta) = (1.52 \pm 0.09)$ nm^{-2}. Subsequently, we performed a quantitative analysis of the oscillations using the standard Lifshitz-Kosevich (LK) formula [49–51],

$$\Delta M \propto -R_D R_T \sin\left\{2\pi\left[\frac{F}{B} - \left(\frac{1}{2} - \phi\right)\right]\right\}, \quad (10)$$

where R_D is the Dingle damping term [$R_D = \exp(2\pi^2 k_B T_D m^*/eB\hbar)$], R_T is the thermal damping factor [$R_T = \frac{2\pi^2 k_B T m^*/eB\hbar}{\sinh(2\pi^2 k_B T m^*/eB\hbar)}$], and $\phi = \phi_B/2\pi - \delta$. Here T_D is the Dingle temperature, k_B is the Boltzmann constant, m^* is the effective electron mass, ϕ_B is the Berry phase, and δ is an additional phase shift that depends on the dimensionality of the FS, i.e., $\delta = 0$ for a two-dimensional (2D) FS and
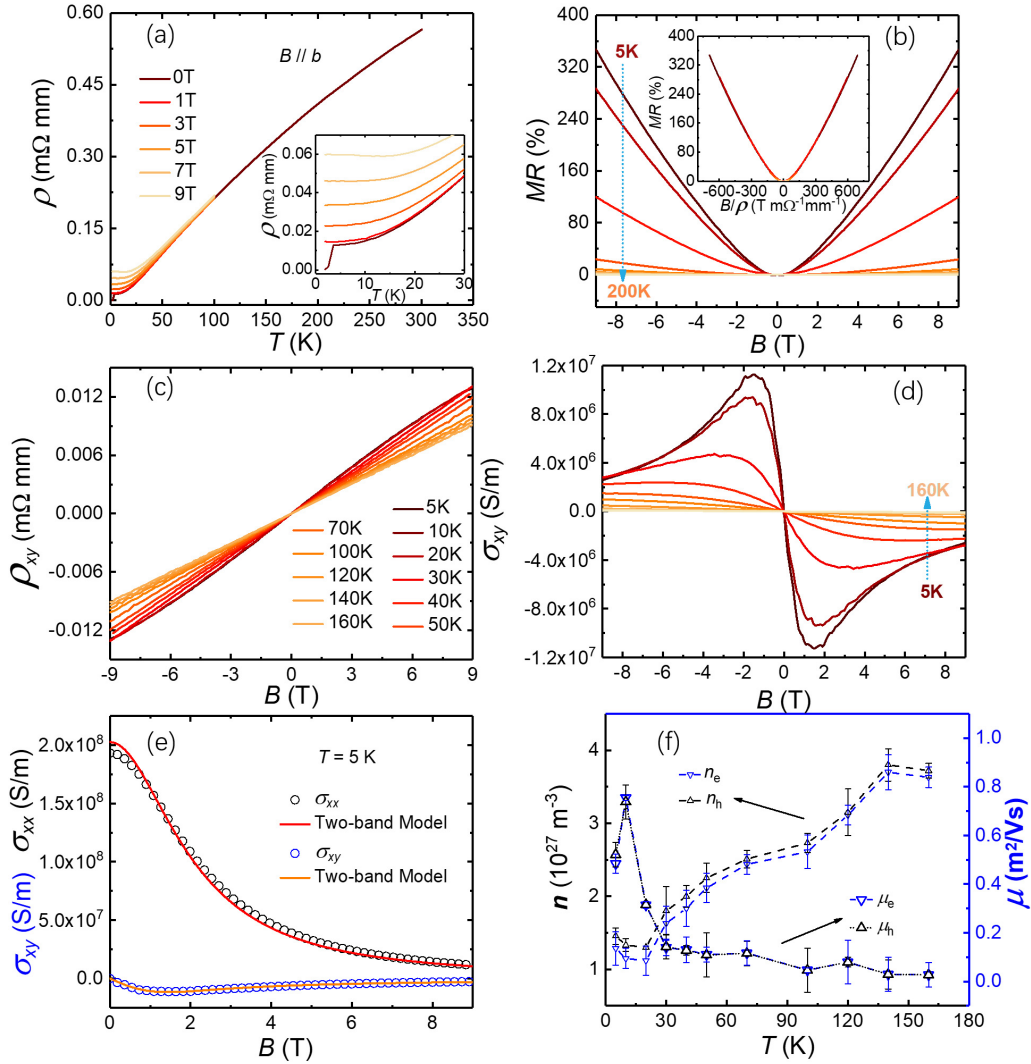
FIG. 3. Temperature dependence of resistivity at some selected fields. Inset: An enlarged view of the low-temperature region. (b) The MR at some fixed temperatures. Inset: The corresponding plot of Kohler's rule. (c) The Hall resistivity ρ_{yx} at some selected temperatures. (d) The Hall conductivity (σ_{xy}) at the same temperatures as indicated in (c). (e) The fits of electrical conductivity σ_{xx} and Hall conductivity σ_{xy} by the two-band model at 5 K. (f) The carrier density and the mobility vs T extracted based on the two-band fitting.

$\delta = \pm\frac{1}{8}$ for a 3D FS [52]. As the Fermi surfaces of PtPb$_4$ are all 3D-like (see below), we only consider $\delta = \pm\frac{1}{8}$ here. As shown in Fig. 4(c), one can determine the effective mass m^* for each frequency by fitting the temperature dependence of the FFT amplitudes to R_T and the fitting yields $m_\alpha = (0.15 \pm 0.01) m_e$ and $m_\beta = (0.27 \pm 0.01) m_e$ (m_e is the bare electron mass). With the above fitted m^*, we can further fit $\Delta M(1/B)$ to the two-band LK formula at 1.9 K to obtain the corresponding Berry phase [see Fig. 4(d)]. The fitting gives the Berry phase and Dingle temperature for each frequency as listed in Table I. For the α band, if we assume $\delta = -\frac{1}{8}$, then $\phi_B = (1.35 \pm 0.08)\pi$, while if we assume $\delta = +\frac{1}{8}$, then $\phi_B = (1.85 \pm 0.11)\pi$. For the β band, the corresponding values are $\phi_B = (1.09 \pm 0.03)\pi$ ($\delta = -\frac{1}{8}$) and $\phi_B = (1.59 \pm 0.05)\pi$ ($\delta = +\frac{1}{8}$), respectively. On the other hand, by applying a band filter, we also implement the single-band LK fitting for each monofrequency oscillation, as shown in Fig. 4(e) for the α and β bands, respectively.

The result from the single-band fitting is nearly the same as that from the two-band LK fitting (Table I). Alternatively, the Berry phase can also be estimated from Landau's fan diagram; as shown in Fig. 4(f), the valleys in the dHvA oscillation were assigned with the Landau level index of $n - 1/4$. From these linear fittings, we obtained $\phi_B = (1.39 \pm 0.17)\pi$ [$\phi_B = (1.89 \pm 0.23)\pi$] for $\delta = -\frac{1}{8}$ ($\delta = +\frac{1}{8}$) for the α band and $\phi_B = (0.89 \pm 0.13)\pi$ [$\phi_B = (1.39 \pm 0.21)\pi$] for $\delta = -\frac{1}{8}$ ($\delta = +\frac{1}{8}$) for the β band, respectively, all of which are consistent with those from the LK fitting. Although the preceding analysis seemingly points to a nontrivial Berry phase in this compound, it should be noted that this phase factor can be complicated by other contributions, such as the Maslov correction and the dynamic phase factor [53–55].

The fermiology of PtPb$_4$ was further studied by the angular dependence of dHvA. From the angle-dependent FFT spectrum [Fig. 4(g)], the angle evolution of the frequency can be tracked. It is evident that both α and β bands are quasi-3D with a small anisotropy. We also found the third
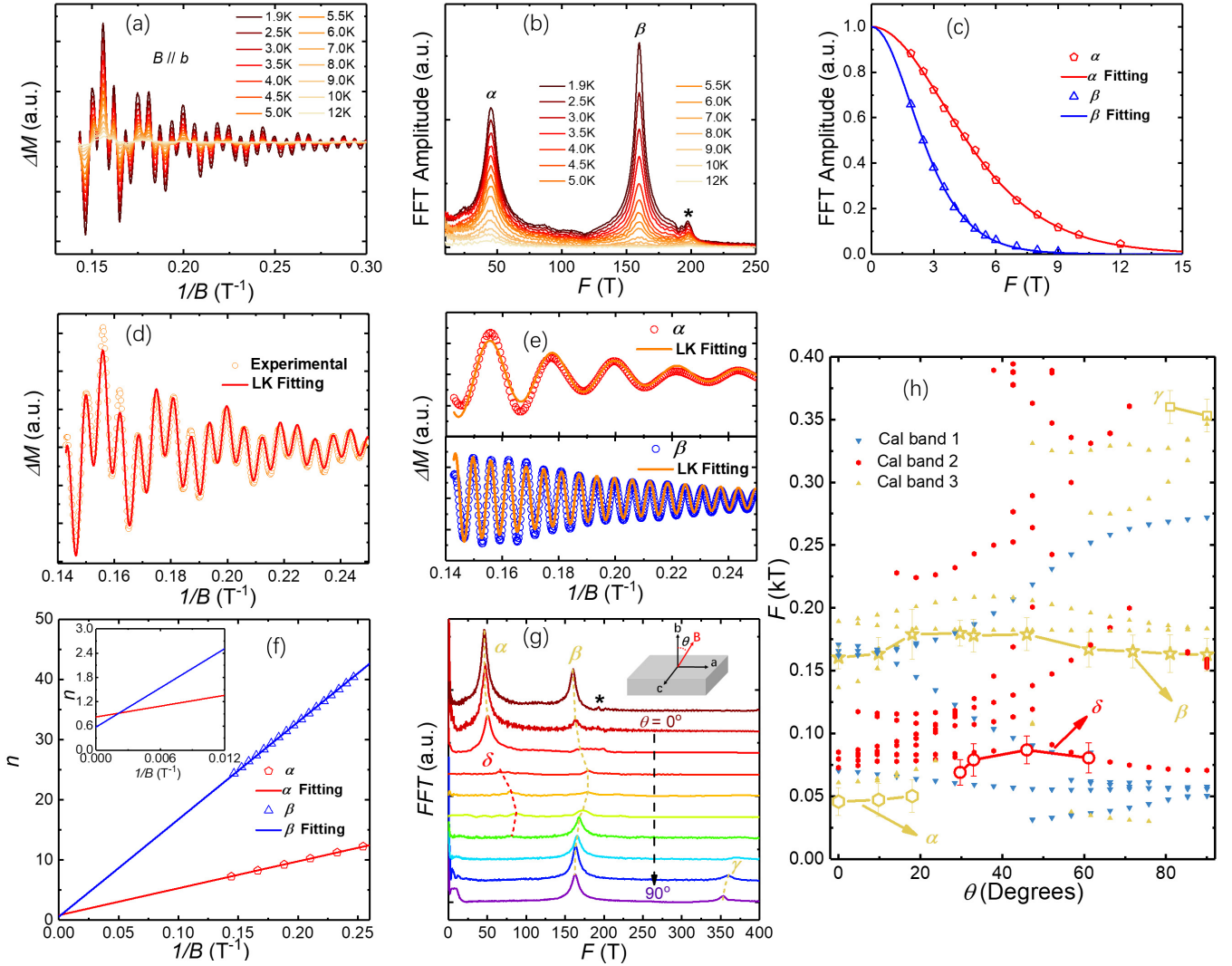
FIG. 4. (a) Oscillatory signals ΔM vs magnetic field B at some selected temperatures after subtracting the background. (b) Fast Fourier transform (FFT) spectra of ΔM oscillations. The asterisk marks the weak peak whose origin is not clear. (c) T dependence of the FFT amplitude. The solid lines are fits to obtain the effective mass for each frequency. (d) The two-band Lifshitz-Kosevich (LK) fitting to the data measured at 1.9 K. (e) The α-band and β-band oscillations were extracted using the FFT filter and fitted with the single-band LK formula. (f) The Landau's fan diagram for α and β. Inset: Enlargement of the interception. (g) Angular dependence of the FFT frequency at 1.9 K. Inset: The rotation schematic diagram. (h) Angular dependence of the FFT frequency from both experiment and calculations. The colors of the α, β, γ, and δ bands are coded per their most likely bands.

frequency $F_\gamma = (353 \pm 13)$ T when the field is applied along the a axis, even though it is weak and fades away quickly with the field angle. Furthermore, to identify the orbital origin of each frequency, we investigated the angle dependence by the first principles. As shown in Fig. 4(h), the frequencies of α and β obtained from experiment may be assigned to band 3,

TABLE I. Parameters obtained from the dHvA oscillations.

Method	Band	F (T)	m^*/m_e	T_D (K)	A (nm^{-2})	$\delta = -\frac{1}{8}$	$\delta = +\frac{1}{8}$
			$H \parallel b$			ϕ_B	
Two-band LK fitting	α	(45 ± 11)	(0.15 ± 0.01)	(10.8 ± 0.65)	(0.43 ± 0.11)	$(1.35 \pm 0.08)\pi$	$(1.85 \pm 0.11)\pi$
	β	(160 ± 9)	(0.27 ± 0.02)	(3.22 ± 0.21)	(1.52 ± 0.09)	$(1.09 \pm 0.03)\pi$	$(1.59 \pm 0.05)\pi$
One-band LK fitting	α	(45 ± 11)	(0.15 ± 0.01)	(9.04 ± 0.81)	(0.43 ± 0.11)	$(1.37 \pm 0.08)\pi$	$(1.87 \pm 0.11)\pi$
	β	(160 ± 9)	(0.27 ± 0.02)	(2.74 ± 0.24)	(1.52 ± 0.09)	$(1.08 \pm 0.03)\pi$	$(1.58 \pm 0.05)\pi$
Landau's fan diagram	α	(45 ± 2)	(0.15 ± 0.01)		(0.43 ± 0.11)	$(1.39 \pm 0.17)\pi$	$(1.89 \pm 0.23)\pi$
	β	(162 ± 3)	(0.27 ± 0.02)		(1.53 ± 0.09)	$(0.89 \pm 0.13)\pi$	$(1.39 \pm 0.21)\pi$
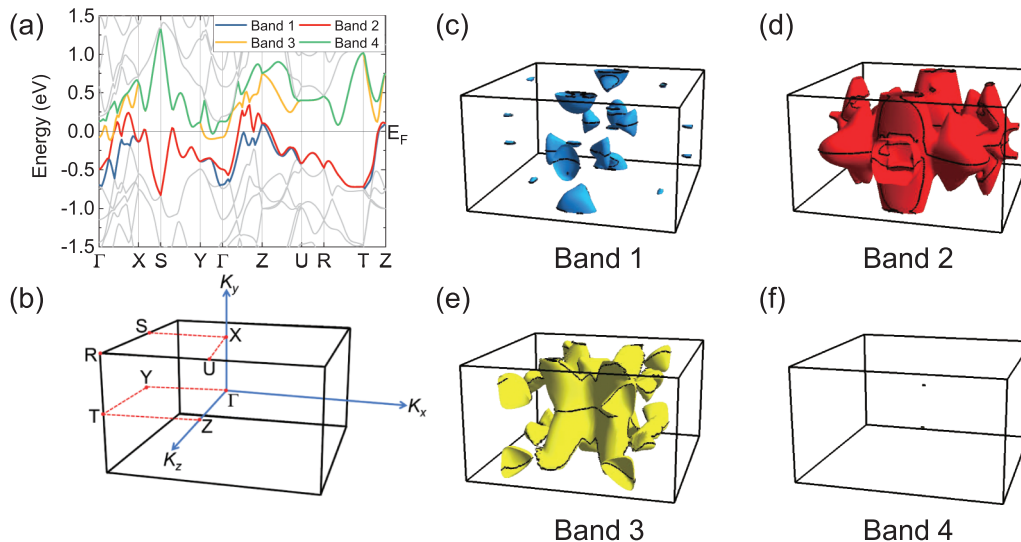
FIG. 5. (a) Calculated band structure for orthorhombic PtPb$_4$ with SOC included. Bands crossing the Fermi level are marked by different colors and labeled by numbers. (b) The Brillouin zone with the high-symmetry points specified. (c–f) The 3D Fermi surfaces for each band. The extremal orbits are illustrated by lines for bands 1–3 when the magnetic field is applied along the b axis.

while the δ band can be assigned to band 2, although outstanding discrepancies between experiment and calculations remain.

To further understand the electronic structure of PtPb$_4$, we perform density functional theory calculations. Following the discussions in Ref. [35], we used an *orthorhombic* structure with centrosymmetric space group $Ccca$ (No. 68) in the band structure calculations, with optimized lattice parameters $a = 6.733$ Å, $b = 11.625$ Å, and $c = 6.672$ Å. The conventional cell of the structure contains 16 Pb atoms and 4 Pt atoms, with stacked Pb-Pt-Pb layers along the b axis. The calculated band structure with SOC is shown in Fig. 5(a). Four bands crossing the Fermi level are illustrated by different colors, where bands 1 and 2 are holelike, and bands 3 and 4 are electronlike. We note that the dispersions along X-S-Y and U-R-T are highly degenerate for band 1 and band 2. It is the same for the dispersions of band 3 and band 4. We also note that the holelike bands and electronlike bands are nearly symmetrical with respect to the Fermi level, especially around the S point. Figure 5(b) shows the Brillouin zone with the high-symmetry points specified and Figs. 5(c)–5(f) resolve the 3D FSs for each band. The FSs of band 1 consist of several small pieces of Fermi pockets. For band 2, the FSs consist of connected barrel-like Fermi pockets surrounding the Brillouin zone center. The FSs of band 3 show a butterflylike pocket in the Brillouin zone center with several small pockets around it, while the FSs of band 4 are composed of two tiny dots. Our results are overall consistent with Lee *et al.*'s work [35]. Although the lattice parameters a and c are very close, the Fermi surfaces demonstrate clear anisotropy along the k_x and k_z directions. To evaluate the possible topologically nontrivial states, we calculated the $\mathbb{Z}_2$ topological invariants on the six time-reversal-invariant momentum planes using the Wannier charge center calculations [56], for both orthorhombic and tetragonal PtPb$_4$ (space group $P4/nbm$; No. 125) where the direct energy gap still appears at every k point, allowing

us to define the topological $\mathbb{Z}_2$ invariant. The $\mathbb{Z}_2$ invariants for orthorhombic PtPb$_4$ are (0; 101), which indicate that orthorhombic PtPb$_4$ exhibits a nontrivial weak topology. As a comparison, the tetragonal PtPb$_4$ is found to be a strong topological insulator with $\mathbb{Z}_2$ (1; 000). A topological phase transition may occur in PtPb$_4$, accompanied by C_4-to-C_2 symmetry breaking. In this sense, the intrinsic superconductivity in PtPb$_4$ ($T_c = 2.7$ K) [36] may provide a natural platform to study the topological superconductivity or topological phase transition in the future.

IV. CONCLUSION

In conclusion, we have presented detailed studies of the transport properties and quantum oscillations of the binary superconductor PtPb$_4$, which is isostructural to the nodal-line semimetal PtSn$_4$. The heat capacity jump at T_c is slightly enhanced compared with the weak-coupling BCS superconductors. The normal-state magnetotransport can overall be described by the two-band model. We have also investigated its possible topological characteristics by the quantum oscillations and density functional theory calculations. The possible nontrivial band topology proposed in this study, along with the large Rashba splitting observed in ARPES [35], makes PtPb$_4$ a plausible venue in which to search for novel superconductivity and spintronic applications. Our findings in this paper provide a simple material platform to look into the potential of intriguing superconductivity and shall motivate more investigations on this material and its derivatives, both theoretically and experimentally.

[1] M. Z. Hasan and C. L. Kane, Topological insulators, Rev. Mod. Phys. **82**, 3045 (2010).

[2] X.-L. Qi and S.-C. Zhang, Topological insulators and superconductors, Rev. Mod. Phys. **83**, 1057 (2011).

[3] A. A. Burkov, Topological semimetals, Nat. Mater. **15**, 1145 (2016).

[4] N. P. Armitage, E. J. Mele, and A. Vishwanath, Weyl and Dirac semimetals in three-dimensional solids, Rev. Mod. Phys. **90**, 015001 (2018).

[5] J. Xiong, K. Satya. Kushwaha, T. Liang, J. W. Krizan, M. Hirschberger, W. D. Wang, R. J. Cava, and N. P. Ong, Evidence for the chiral anomaly in the Dirac semimetal Na_3Bi, Science **350**, 413 (2015).

[6] D. X. Qu, Y. S. Hor, J. Xiong, R. J. Cava, and N. P. Ong, Quantum oscillations and Hall anomaly of surface states in the topological insulator Bi_2Te_3, Science **329**, 821 (2010).

[7] M. N. Ali, J. Xiong, S. Flynn, J. Tao, Q. D. Gibson, L. M. Schoop, T. Liang, N. Haldolaarachchige, M. Hirschberger, N. P. Ong, and R. J. Cava, Large, non-saturating magnetoresistance in WTe_2, Nature (London) **514**, 205 (2014).

[8] X. C. Huang, L. X. Zhao, Y. J. Long, P. P. Wang, D. Chen, Z. H. Yang, H. Liang, M. Q. Xue, H. M. Weng, Z. Fang, X. Dai, and G. F. Chen, Observation of the Chiral-Anomaly-Induced Negative Magnetoresistance in 3D Weyl Semimetal TaAs, Phys. Rev. X **5**, 031023 (2015).

[9] B. Q. Lv, H. M. Weng, B. B. Fu, X. P. Wang, H. Miao, J. Ma, P. Richard, X. C. Huang, L. X. Zhao, G. F. Chen, Z. Fang, X. Dai, T. Qian, and H. Ding, Experimental Discovery of Weyl Semimetal TaAs, Phys. Rev. X **5**, 031013 (2015).

[10] C. Shekhar, A. K. Nayak, Y. Sun, M. Schmidt, M. Nicklas, I. Leermakers, U. Zeitler, Y. Skourski, J. Wosnitza, Z. K. Liu, Y. L. Chen, W. Schnelle, H. Borrmann, Y. Grin, C. Felser, and B. H. Yan, Extremely large magnetoresistance and ultrahigh mobility in the topological Weyl semimetal candidate NbP, Nat. Phys. **11**, 645 (2015).

[11] Y. F. Zhao, H. W. Liu, C. L. Zhang, H. C. Wang, J. F. Wang, Z. Q. Lin, Y. Xing, H. Lu, J. Liu, Y. Wang, S. M. Brombosz, Z. L. Xiao, S. Jia, X. C. Xie, and J. Wang, Anisotropic Fermi Surface and Quantum Limit Transport in High Mobility Three-Dimensional Dirac Semimetal Cd_3As_2, Phys. Rev. X **5**, 031037 (2015).

[12] A. Narayanan, M. D. Watson, S. F. Blake, N. Bruyant, L. Drigo, Y. L. Chen, D. Prabhakaran, B. Yan, C. Felser, T. Kong, P. C. Canfield, and A. I. Coldea, Linear Magnetoresistance Caused by Mobility Fluctuations in N-Doped Cd_3As_2, Phys. Rev. Lett. **114**, 117201 (2015).

[13] H. Li, H. T. He, H. Z. Lu, H. C. Zhang, H. C. Liu, R. Ma, Z. Y. Fan, S. Q. Shen, and J. N. Wang, Negative magnetoresistance in Dirac semimetal Cd_3As_2, Nat. Commun. **7**, 10301 (2016).

[14] X. L. Liu, H. Y. Wang, H. Su, Z. H. Yu, and Y. F. Guo, Nontrivial topological states in the tantalum dipnictides TaX_2 (X = As, P), Tungsten **2**, 251 (2020).

[15] M. N. Ali, M. Schoop, C. Garg, J. M. Lippmann, E. Lara, B. Lotsch, and S. S. P. Parkin, Butterfly magnetoresistance, quasi-2D Dirac Fermi surface and topological phase transition in ZrSiS, Sci. Adv. **2**, e1601742 (2016).

[16] L. M. Schoop, M. N. Ali, C. Straßer, A. Topp, A. Varykhalov, D. Marchenko, V. Duppel, S. Parkin, B. V. Lotsch, and C. R. Ast, Dirac cone protected by non-symmorphic symmetry and three-dimensional Dirac line node in ZrSiS, Nat. Commun. **7**, 11696 (2016).

[17] M. Neupane, I. Belopolski, M. M. Hosen, D. S. Sanchez, R. Sankar, M. Szlawska, S. Y. Xu, K. Dimitri, N. Dhakal, P. Maldonado, P. M. Oppeneer, D. Kaczorowski, F. C. Chou, M. Z. Hasan, and T. Durakiewicz, Observation of topological nodal fermion semimetal phase in ZrSiS, Phys. Rev. B **93**, 201104(R) (2016).

[18] B. B. Fu, C. J. Yi, T. T. Zhang, M. Caputo, J. Z. Ma, X. Gao, B. Q. Lv, L. Y. Kong, Y. B. Huang, P. Richard, M. Shi, V. N. Strocov, C. Fang, H. M. Weng, Y. G. Shi, T. Qian, and H. Ding, Dirac nodal surfaces and nodal lines in ZrSiS, Sci. Adv. **5**, eaau6459 (2019).

[19] G. Bian, T. R. Chang, R. Sankar, S. Y. Xu, H. Zheng, T. Neupert, C. K. Chiu, S. M. Huang, G. Q Chang, I. Belopolski, D. S. Sanchez, M. Neupane, N. Alidoust, C. Liu, B. K. Wang, C. C. Lee, H. T. Jeng, C. L. Zhang, Z. J. Yuan, S. Jia, A. Bansil, F. C. Chou *et al.*, Topological nodal-line fermions in spin-orbit metal $PbTaSe_2$, Nat. Commun. **7**, 10556 (2016).

[20] S. Y. Guan, P. J. Chen, M. W. Chu, R. Sankar, F. C. Chou, H. T. Jeng, C. S. Chang, and T. M. Chuang, Superconducting topological surface states in the noncentrosymmetric bulk superconductor $PbTaSe_2$, Sci. Adv. **2**, e1600894 (2016).

[21] Y. Wu, L. L. Wang, E. Mun, D. D. Johnson, D. X. Mou, L. N. Huang, Y. B. Lee, S. L. Bud'ko, P. C. Canfield, and A. Kaminski, Dirac node arcs in $PtSn_4$, Nat. Phys. **12**, 667 (2016).

[22] G. W. Li, C. G. Fu, W. J. Shi, L. Jiao, J. Q. Wu, Q. Yang, R. Saha, M. E. Kamminga, A. K. Srivastava, E. Liu, A. N. Yazdani, N. Kumar, J. Zhang, G. R. Blake, X. J. Liu, M. Fahlman, S. Wirth, G. Auffermann, J. Gooth, S. Parkin *et al.*, Dirac nodal arc semimetal $PtSn_4$: An ideal platform for understanding surface properties and catalysis for hydrogen evolution, Angew. Chem. **131**, 13241 (2019).

[23] L. Fu and E. Berg, Odd-Parity Topological Superconductors: Theory and Application to $Cu_xBi_2Se_3$, Phys. Rev. Lett. **105**, 097001 (2010).

[24] R. Joynt and L. Taillefer, The superconducting phases of UPt_3, Rev. Mod. Phys. **74**, 235 (2002).

[25] P. K. Biswas, S. K. Ghosh, J. Z. Zhao, D. A. Mayoh, N. D. Zhigadlo, X. Xu, C. Baines, A. D. Hillier, G. Balakrishnan, and M. R. Lees, Chiral singlet superconductivity in the weakly correlated metal LaPt$_3$P, Nat. Commun. **12**, 2504 (2021).

[26] M. Sato and Y. Ando, Topological superconductors: A review, Rep. Prog. Phys. **80**, 076501 (2017).

[27] P. Das, Y. Suzuki, M. Tachiki, and K. Kadowak, Spin-triplet vortex state in the topological superconductor Cu$_x$Bi$_2$Se$_3$, Phys. Rev. B **83**, 220513(R) (2011).

[28] K. Matano, M. Kriener, K. Segawa, Y. Ando, and G.-q. Zheng, Spin-rotation symmetry breaking in the superconducting state of Cu$_x$Bi$_2$Se$_3$, Nat. Phys. **12**, 852 (2016).

[29] L. M. Schoop, L. S. Xie, R. Chen, Q. D. Gibson, S. H. Lapidus, I. Kimchi, M. Hirschberger, N. Haldolaarachchige, M. N. Ali, C. A. Belvin, T. Liang, J. B. Neaton, N. P. Ong, A. Vishwanath, and R. J. Cava, Dirac metal to topological metal transition at a structural phase change in Au$_2$Pb and prediction of $\mathbb{Z}_2$ topology for the superconductor, Phys. Rev. B **91**, 214517 (2015).

[30] Y. Wu, G. Drachuck, L. L. Wang, D. D. Johnson, P. Swatek, B. Schrunk, D. X. Mou, L. N. Huang, S. L. Bud'ko, P. C. Canfield, and A. Kaminski, Electronic structure of the topological superconductor candidate Au$_2$Pb, Phys. Rev. B **98**, 161107(R) (2018).

[31] T. Le, Y. Sun, H. K. Jin, L. Che, L. Yin, J. Li, G. M. Pang, C. Q. Xu, L. X. Zhao, S. Kittaka, T. Sakakibara, K. Machida, R. Sankar, H. Q. Yuan, G. F. Chen, X. Xu, S. Li, Y. Zhou, and X. Lu, Evidence for nematic superconductivity of topological surface states in PbTaSe$_2$, Sci. Bull. **65**, 1349 (2020).

[32] K. Iwaya, Y. Kohsaka, K. Okawa, T. Machida, M. S. Bahramy, T. Hanaguri, and T. Sasagawa, Full-gap superconductivity in spin-polarised surface states of topological semimetal β-PdBi$_2$, Nat. Commun. **8**, 976 (2017).

[33] Y. Li, S. J. Yang, D. L. Sun, Y. B. Sun, Y. Li, E. Vetter, R. Sun, N. Li, X. Yang, L. Su, Z. Z. Gong, Z. K. Xie, J. J. Zhao, W. He, X. Q. Zhang, and Z. H. Cheng, Large spin to charge conversion in the topological superconductor β-PdBi$_2$ at room temperature, Phys. Rev. B **102**, 014420 (2020).

[34] Y. Li, Q. Gu, C. Chen, J. Zhang, Q. Liu, X. Hu, J. Liu, Y. Liu, L. Li, M. Tian, Y. Wang, N. Samarth, S. Li, T. Zhang, J. Feng, and J. Wang, Nontrivial superconductivity in topological MoTe$_{2-x}$S$_x$ crystals, Proc. Natl. Acad. Sci. USA **115**, 9503 (2018).

[35] K. Lee, D. Mou, N. H. Jo, Y. Wu, B. Schrunk, J. M. Wilde, A. Kreyssig, A. Estry, S. L. Bud'ko, M. C. Nguyen, L. L. Wang, C. Z. Wang, K. M. Ho, P. C. Canfield, and A. Kaminski, Evidence for large Rashba splitting in PtPb$_4$ from angle-resolved photoemission spectroscopy, Phys. Rev. B **103**, 085125 (2021).

[36] M. Gendron and R. Jones, Superconductivity in the CuAl$_2$ (C16) crystal class, J. Phys. Chem. Solids **23**, 405 (1962).

[37] Z. Wu and R. E. Cohen, More accurate generalized gradient approximation for solids, Phys. Rev. B **73**, 235116 (2006).

[38] K. Schwarz, P. Blaha, and G. K. H. Madsen, Electronic structure calculations of solids using the WIEN2k package for material sciences, Comput. Phys. Commun. **147**, 71 (2002).

[39] A. A. Mostofi, J. R. Yates, G. Pizzi, Y. S. Lee, I. Souza, D. Vanderbilt, and N. Marzari, An updated version of WANNIER90: A tool for obtaining maximally-localised Wannier functions, Comput. Phys. Commun. **185**, 2309 (2014).

[40] Q. S. Wu, S. N. Zhang, H. F. Song, M. Troyer, and A. A. Soluyanov, WannierTools: An open-source software package for novel topological materials, Comput. Phys. Commun. **224**, 405 (2018).

[41] P. M. C. Rourke and S. R. Julian, Numerical extraction of de Haas–van Alphen frequencies from calculated band energies, Comp. Phys. Commun. **183**, 324 (2012).

[42] J. F. Mercure, A. F. Bangura, X. Xu, N. Wakeham, A. Carrington, P. Walmsley, M. Greenblatt, and N. E. Hussey, Upper Critical Magnetic Field Far Above the Paramagnetic Pair-Breaking Limit of Superconducting One-Dimensional Li$_{0.9}$Mo$_6$O$_{17}$ Single Crystals, Phys. Rev. Lett. **108**, 187003 (2012).

[43] J. P. Carbotte, Properties of boson-exchange superconductors, Rev. Mod. Phys. **62**, 1027 (1990).

[44] N. R. Werthamer, E. Helfand, and P. C. Hohenberg, Temperature and purity dependence of the superconducting critical field, H$_{c2}$. III. Electron spin and spin-orbit effects, Phys. Rev. **147**, 295 (1966).

[45] Y. L. Wang, L. R. Thoutam, Z. L. Xiao, J. Hu, S. Das, Z. Q. Mao, J. Wei, R. Divan, A. Luican-Mayer, G. W. Crabtree, and W. K. Kwok, Origin of the turn-on temperature behavior in WTe$_2$, Phys. Rev. B **92**, 180402(R) (2015).

[46] N. H. Jo, Y. Wu, L. L. Wang, P. P. Orth, S. S. Downing, S. Manni, D. Mou, D. D. Johnson, A. Kaminski, S. L. Bud'ko, and P. C. Canfield, Extremely large magnetoresistance and Kohler's rule in PdSn$_4$: A complete study of thermodynamic, transport, and band-structure properties, Phys. Rev. B **96**, 165145 (2017).

[47] G. Grosso and G. P. Parravicini, *Solid State Physics* (Academic Press, New York, 2000).

[48] J. Xu, N. J. Ghimire, J. S. Jiang, Z. L. Xiao, A. S. Botana, Y. L. Wang, Y. Hao, J. E. Pearson, and W. K. Kwok, Origin of the extremely large magnetoresistance in the semimetal YSb, Phys. Rev. B **96**, 075159 (2017).

[49] I. M. Lifshits and A. M. Kosevich, Theory of magneticsusceptibility in metals at low temperature, Sov. Phys. JETP **2**, 636 (1956).

[50] G. P. Mikitik and Y. V. Sharlai, Manifestation of Berry's Phase in Metal Physics, Phys. Rev. Lett. **82**, 2147 (1999).

[51] Amit, R. K. Singh, N. Wadehra, S. Chakraverty, and Y. Singh, Type-II Dirac semimetal candidates ATe$_2$ (A = Pt, Pd): A de Haas–van Alphen study, Phys. Rev. Mater. **2**, 114202 (2018).

[52] C. Li, C. M. Wang, B. Wan, X. Wan, H.-Z. Lu, and X. C. Xie, Rules for Phase Shifts of Quantum Oscillations in Topological Nodal-Line Semimetals, Phys. Rev. Lett. **120**, 146602 (2018).

[53] A. Alexandradinata, C. Wang, W. Duan, and L. Glazman, Revealing the Topology of Fermi-Surface Wave Functions from Magnetic Quantum Oscillations, Phys. Rev. X **8**, 011027 (2018).

[54] A. Alexandradinata and L. Glazman, Semiclassical theory of Landau levels and magnetic breakdown in topological metals, Phys. Rev. B **97**, 144422 (2018).

[55] C. Schindler, D. Gorbunov, S. Zherlitsyn, S. Galeski, M. Schmidt, J. Wosnitza, and J. Gooth, Strong anisotropy of the electron-phonon interaction in NbP probed by magnetoacoustic quantum oscillations, Phys. Rev. B **102**, 165156 (2020).

[56] A. A. Soluyanov and D. Vanderbilt, Computing topological invariants without inversion symmetry, Phys. Rev. B **83**, 235401 (2011).